Wi-Painter: Fine-grained Material Identification and Image Delineation Using COTS WiFi Devices

DAWEI YAN, University of Science and Technology of China, China
PANLONG YANG*, Nanjing University of Information Science and Technology, China
FEI SHANG, University of Science and Technology of China, China
WEIWEI JIANG, Nanjing University of Information Science and Technology, China
XIANG-YANG LI, University of Science and Technology of China, Deqing Alpha Innovation Institute, China

WiFi has gradually developed into one of the main candidate technologies for indoor environment sensing. In this paper, we are interested in using COTS WiFi devices to identify material details, including location, material type, and shape, of stationary objects in the surrounding environment, which may open up new opportunities for many applications. Specifically, we present *Wi-Painter*, a model-driven system that can accurately detects smooth-surfaced material types and their edges using COTS WiFi devices without modification. Different from previous arts for material identification, *Wi-Painter* subdivides the target into individual 2D pixels, and simultaneously forms a 2D image based on identifying the material type of each pixel. The key idea of *Wi-Painter* is to exploit the complex permittivity of the object surface which can be estimated by the different reflectivity of signals with different polarization directions. In particular, we construct the multi-incident angle model to characterize the material, using only the power ratios of the vertically and horizontally polarized signals measured at several different incident angles, which avoids the use of inaccurate WiFi signal phases. We implement and evaluate *Wi-Painter* in the real world, showing an average classification accuracy of 93.4% for different material types including metal, wood, rubber and plastic of different sizes and thicknesses, and across different environments. In addition, *Wi-Painter* can accurately detect the material type and edge of the word "LOVE" spliced with different materials, with an average size of $60cm \times 80cm$, and material edges with different orientations.

CCS Concepts: • **Human-centered computing** → **Ubiquitous and mobile computing design and evaluation methods**.

Additional Key Words and Phrases: Wireless sensing; Material identification; Object imaging; Complex permittivity.

*Corresponding Author

Authors' addresses: Dawei Yan, yandw@mail.ustc.edu.cn, University of Science and Technology of China, No. 96 Jinzhai Road, Hefei, Anhui, China, 230027; Panlong Yang, plyang@ustc.edu.cn, Nanjing University of Information Science and Technology, No. 219 Ningliu Road, Nanjing, Jiangsu, China, 210044; Fei Shang, shf_1998@outlook.com, University of Science and Technology of China, No. 96 Jinzhai Road, Hefei, Anhui, China, 230027; Weiwei Jiang, weiweijiangcn@gmail.com, Nanjing University of Information Science and Technology, No. 219 Ningliu Road, Nanjing, Jiangsu, China, 210044; Xiang-Yang Li, xiangyangli@ustc.edu.cn, University of Science and Technology of China, Deqing Alpha Innovation Institute, No. 96 Jinzhai Road, Hefei, Anhui, China, 230027.
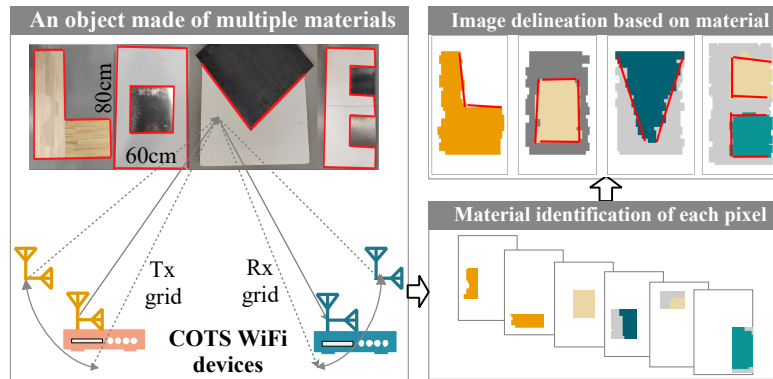
Fig. 1. In real scenarios, an object may consist of multiple different materials, and identification of material details may open up new opportunities for many applications. *Wi-Painter* utilizes COTS WiFi devices with horizontally and vertically polarized signals to achieve fine-grained material identification, further enabling image delineation.
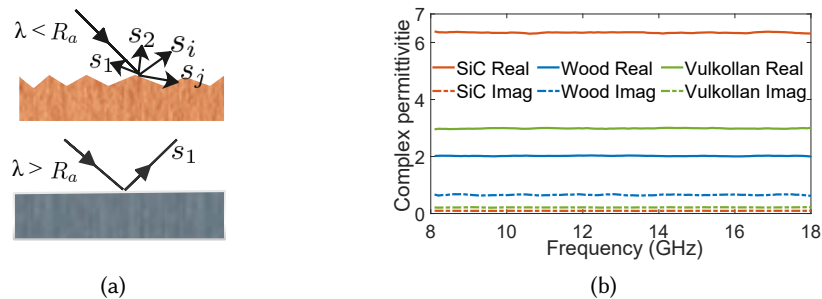

Fig. 2. *Limitations of material identification based on scattering and frequency features:* (a) More quasi-specular (bottom) rather than diffuse (top) at low frequency, resulting in less backscattering features, where R_a is the surface roughness, and s_i, s_j are the scattering signals. (b) The complex permittivities of solid materials vary little with frequency in the GHz band.

1 INTRODUCTION

Motivation. Due to its ubiquity and low cost, WiFi is developing as a prime candidate for indoor environmental sensing. In recent years, WiFi signals have been used for people tracking [25, 32, 42, 59, 60], health monitoring [34, 36, 50, 68], object imaging [20, 31, 39, 41], and material identification [15, 43, 56, 66]. In general, identifying materials for objects in environments is important for many applications. For example, identifying the material of a metal surface can tell user whether it is corroded [26], or the soil type can be judged by measuring the water content [10, 24]. Fine-grained liquid detection can identify fake perfume and wine [17, 21]. If the robot or drone can detect the material of surrounding objects [66], this can be used for search and rescue, parking assistance and *etc.*While cameras can identify materials, it cannot do so under *non line of sight* (NLoS) and requires highlights, and more importantly, cannot differentiate between similar-looking materials. Therefore, if we can identify details of materials using *commercial-off-the-shelf* (COTS) WiFi devices, it can open up new opportunities for many applications.

Prior arts and their limitations. From previous work, it is feasible to use reflected or transmitted RF signals for material identification, which can be achieved by extracting rich scattering features related to materials [55, 66,

69]. These material identification systems treat each object as a separate entity, and the accuracy of material identification based on feature extraction decreases as the surface area of the object decreases. However, in the real environment, many objects may be close together (*e.g.*, books and metal ornaments placed on a bookshelf), or an object is composed of many different materials (*e.g.*, table with wooden planks above and metal below), as shown in Fig. 1. While there are some RF imaging systems, the boundaries of these objects cannot be well demarcated when the materials are similar. In addition, since WiFi signal wavelengths greater than the roughness of the object surface, quasi-specular reflections occur instead of informative diffuse reflections [39], as shown in Fig. 2a. This makes schemes based on scattering features unsuitable for distinguishing similarly smooth-surfaced materials.

There are also some works utilizing the complex permittivity to identify materials, since different materials exhibit different complex permittivities [44, 45, 48]. These works use the relationship between complex permittivity and frequency to construct features that can identify materials, but the accuracy is affected by the bandwidth, and the performance is poor when using COTS WiFi devices. What's more, as shown in Fig. 2b, the complex permittivity of many solids varies very little with frequency, which makes the scheme of constructing features based on frequency failed. Therefore, material identification details using COTS WiFi devices remains a challenging problem.

Key idea. An important observation is that after incident waves with different polarization directions are reflected by the object, the reflectivity of the object is different, which is related to the complex permittivity. Therefore, by exploiting the different reflectivity of the object for signals with different polarization directions, we can directly estimate the complex permittivity of the object surface to identify different materials. In this way, there is no need for rich scattering features on the surface of the object, and this can be achieved using COTS WiFi devices without modification (*e.g.*, $5GHz/40MHz$). We further subdivide the reflected surface into many small reflected areas and measure the complex permittivity of each reflected area individually, thereby distinguishing the edges of different materials.

Challenges. Although the polarimetry has been widely used in the remote sensing literature [29], generalizing it to COTS WiFi signals for fine-grained measurement of the complex permittivity still faces the following challenges:

- *How to fine-grained estimate the complex permittivity of material when WiFi signal phase measurement is inaccurate?* Estimating the complex permittivity using polarization methods usually requires accurate measurement of the amplitude and the phase of the reflected signal from the material. However, the acquisition of signal phase is affected by many factors, such as *sampling frequency offset* (SFO), *time of fight* (ToF) and *etc.*, resulting in large error of the estimated complex permittivity using the amplitude and phase. So how to fine-grainedly estimate the complex permittivity of material using only the accurate signal amplitude?

- *How to use COTS WiFi to mark reflected areas with centimeter-level accuracy?* Before analyzing the properties of the material, it is necessary to separate the signals reflected from of each material in space, and mark the same reflected area with centimeter-level accuracy. Since we use reflected signals, we cannot traditionally use multiple *angle of arrival* (AoA) or propagation distances to achieve precise localization, and the WiFi bandwidth is not enough to support us to directly use ToF to separate multipath signals. So how to accurately obtain these parameters from WiFi signals undergoing multipath propagation?

- *How to remove the influences of other items related to materials and edges detection accuracy?* An object may be composed of several different materials and have their sizes. When the reflected area is located at the junction of two different materials, or there is a large error in the reflection path parameter estimation in some reflected areas, these lead to material identification errors or position marking errors, which will affect edge detection. So how to effectively deal with these problems?

Our methods. To address the above challenges, we present *Wi-Painter*, a scheme for fine-grained measurements of materials and edges of unknown objects' surfaces in the environment based on orthogonally polarized WiFi signals.

(i) Firstly, to solve the problem of accurately estimating the complex permittivity using only the amplitude of WiFi signals in orthogonally polarized channels, we establishe the multi-incident angle model. We observe that the reflectance varies depending on the incident angle of the signal reaching the surface. Therefore, we measure the power ratio of the orthogonally polarized signals at different incident angles, and traverse the phase difference in the range of $[0, 2\pi]$ to establish the relationship between the real part and the imaginary part of the complex permittivity, and these relationships will tend to a certain point , which is the value of the complex permittivity.

(ii) Secondly, based on the multipath model represented by the parameters of *angle of departure* (AoD), AoA, attenuation, and path delay, the parameters of each path are preliminarily estimated. We then build the equal-complementary angle model using geometric principle, to achieve centimeter-level marking of reflected areas. Specifically, we consider that within a reflected area of the material, its relative orientation to the WiFi transceiver is equal to half the sum of the measured AoD and AoA. We establish constraints by moving the transceiver or the object material (moving window equal to the reflected region) to enhance the multipath separation, get the power ratio of the orthogonally polarized signals of each reflection path, and use the refined parameters to calculate the position and orientation of each reflected area.

(iii) Thirdly, aiming at fine-grained identification of different materials and edges, we extend the reflected area to 2D, refer to the idea of *polarimetric synthetic aperture rada* (PolSAR) imaging, take the orthogonally polarized signals of multiple incident angles as image pixels, and then calculate the coordinates of each pixel and its material type. In order to deal with the strong speckle in the image, we build Gaussian shaped filter to judge whether it is an edge or not according to the difference between the two sides of the central pixel, and fit successive edge pixels of the same material to outline the accurate material edge.

Contributions. Overall, the main contributions of this paper are as follows:

- We propose *Wi-Painter*, to the best of our knowledge, the first model-driven attempt to perform fine-grained identification of not only materials but also edges using COTS WiFi devices. The advantage of *Wi-Painter* is that the smooth-surfaced material types and their edges can be detect accurately without the prior data of the target materials and without the need for the WiFi transceiver to perform high-bandwidth scans.
- We construct multi-incident angle model, only measure several power ratios of orthogonally polarized signals at different incident angles to characterize the material of the reflected area. We build equal-complementary angle model and establish constraints to enhance multipath separation, and use refinement parameters to obtain the location of each reflected area and the power ratio of the orthogonally polarized signals. We also bulid Gaussian shaped filter and fit successive reflected areas of the same material to improve accuracy.
- We implement *Wi-Painter* based on four WiFi network interface cards (NICs) IWL5300 with independent vertically polarized and horizontally polarized antennas, and move the transceiver or target materials to construct antenna grids. We test our proposed models and techniques in real world, for different material types, sizes, thicknesses, and environments, achieving an average classification accuracy of 93.4%. In addition, *Wi-Painter* can accurately detect the material types and edges of the word "LOVE" spliced with different materials.

The rest of this paper is organized as follows: Section 2 presents some preliminaries of the polarized electro-magnetic waves, the basic method of estimating the object surface's complex permittivity using the orthogonally polarized signals and the basic Principles of PolSAR Imaging. We show the overview of *Wi-Painter* in Section 3. In Section 4, Section 5 and Section 6, we describe the proposed model and techniques for fine-grained estimation

of object materials and their edges in details. Implementation and evaluation are presented in Section 7 and Section 8. We discuss more about the performance and limitations of *Wi-Painter* in Section 9. Section 10 discusses the related works. We finally conclude our work in Section 11.
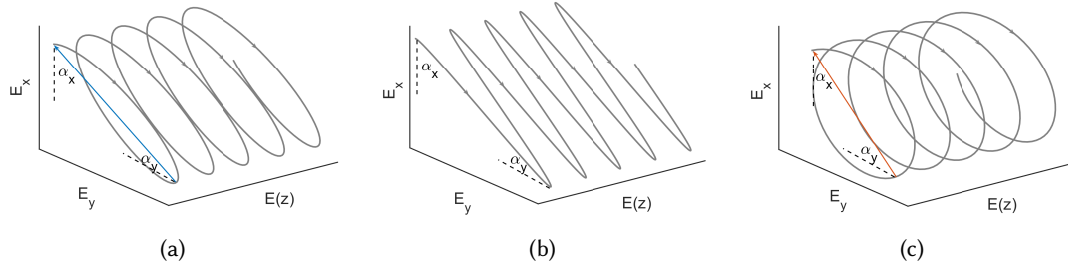

Fig. 3. *Propagation of polarized electromagnetic plane waves:* (a) elliptical polarization, (b) linear polarization, (c) circular polarization.

2 PRELIMINARIES

2.1 Propagation and Reflection of Polarized Electromagnetic Waves

The electric and magnetic fields of an electromagnetic plane wave are perpendicular to each other and to the direction of propagation. The complex electric field of an electromagnetic plane wave propagating along the z direction can be expressed as [5]:

$$
\begin{aligned}
\hat{\vec{E}}(z) &= \hat{a}_x \hat{E}_x(z) + \hat{a}_y \hat{E}_y(z) \\
&= \hat{a}_x E_x e^{-j(\kappa z - \alpha_x)} + \hat{a}_y E_y e^{-j(\kappa z - \alpha_y)}
\end{aligned}
\tag{1}
$$

where $\hat{a}_x$ and $\hat{a}_y$ are the complex amplitudes, $\hat{E}_x(z)$ and $\hat{E}_y(z)$ are the electric field components in the x and y directions, α_x and α_y are the angles between the two electric field components and x and y directions, κ is a parameter. In general, the polarization direction of electromagnetic wave refers to the polarization direction of the electric field [52]. Fig. 3 shows the three polarization modes of electromagnetic waves. If the electric field oscillates in only one direction, it is linearly polarized [5, 22], as shown in Fig. 3b. The most common linear polarizations are horizontal polarization ($\alpha_y = 0°$) and vertical polarization ($\alpha_x = 0°$), as shown in Fig. 4 (left).

Considering a linearly polarized electromagnetic plane wave, different reflections and transmissions will occur when it propagates from air to other medium [16]. As shown in Fig. 4 (right), the x-axis is the interface, the xoz plane is the incident plane, α is the incident angle. $I_\parallel$ and $I_\perp$ are the electric field components of the incident waves parallel and perpendicular to the incident plane, and $R_\parallel$ and $R_\perp$ are the electric field components of the reflected waves parallel and perpendicular to the incident plane, respectively. It is worth noting that the components of the reflected wave differ due to the complex permittivity, and different materials have different complex permittivities [40, 44, 45, 48], which is the physical principle behind using complex permittivity to identify different materials.
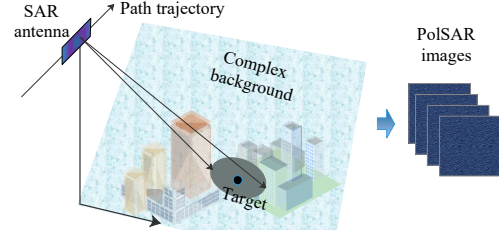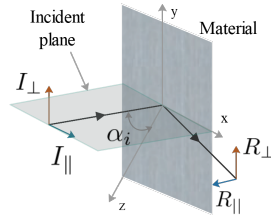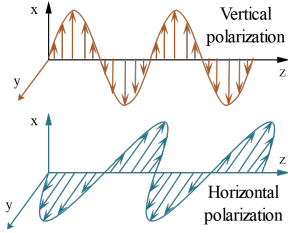
Fig. 4. Propagation (left) and reflection (right) of linearly polarized electromagnetic waves.

Fig. 5. Polarimetric synthetic aperture radar imaging.

2.2 Polarimetry for Determining the Complex Permittivity

The reflection coefficient can be expressed as the amplitude ratio of the reflected wave to the incident wave [16]. Assuming that the linearly polarized electromagnetic plane waves parallel and perpendicular to the incident surface are obliquely incident from the air to the medium, we can obtain the Fresnel reflection coefficients as following [2, 35]:

$$\mathfrak{R}_{hp} = \frac{\cos\alpha - \sqrt{\varepsilon - \sin^2\alpha}}{\cos\alpha + \sqrt{\varepsilon - \sin^2\alpha}}, \tag{2}$$

$$\mathfrak{R}_{vp} = -\frac{\varepsilon\cos\alpha - \sqrt{\varepsilon - \sin^2\alpha}}{\varepsilon\cos\alpha + \sqrt{\varepsilon - \sin^2\alpha}}, \tag{3}$$

where $\mathfrak{R}_{hp}$ and $\mathfrak{R}_{vp}$ are the reflection coefficients for horizontal and vertical polarization, and ε is the complex permittivity. However, it is difficult to directly measure the reflection coefficient of an unknown medium, and usually the amplitude and phase of the signal can be obtained. Furthermore, taking the ratio of the two reflection coefficients obtained by the orthogonal polarization as:

$$\mathcal{P} = \frac{\mathfrak{R}_{vp}}{\mathfrak{R}_{hp}} = |\mathcal{P}|e^{j\Psi}. \tag{4}$$

Obviously $\mathcal{P}$ is a complex number, that is, it not only depends on the power ratio of the signal, but also depends on the phase difference of the receiver orthogonally polarized signal. Then, we can get the complex permittivity [35]:

$$\varepsilon = \left[1 + \frac{4\mathcal{P}}{(1-\mathcal{P})^2}\sin^2\alpha\right]\tan^2\alpha. \tag{5}$$

In theory, the above method can measure the complex permittivity very accurately, so as to identify the material well. However, there are still many problems in using WiFi signals to achieve fine-grained material recognition, which we explain in Section 4.

2.3 Polarimetric Synthetic Aperture Radar Imaging

PolSAR has been widely used in the fields of object classification, environmental monitoring, and target detection [12, 18, 29]. As shown in Fig. 5, PolSAR obtains the polarization scattering matrix of the target by transmitting and receiving electromagnetic waves with different polarization directions, and then studies the polarization scattering characteristics of different objects [8, 38]. At present, PolSAR is divided into polarization systems such as single polarization, dual polarization, and full polarization.
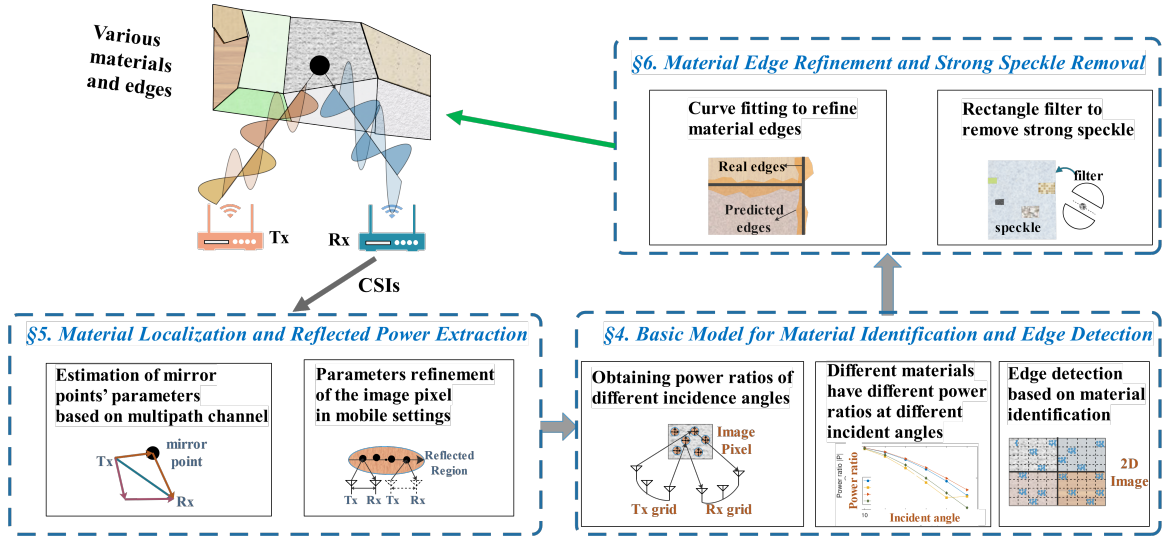
Fig. 6. System overview: *Wi-Painter* takes as input the CSI measurements of the receiver during movement of the WiFi transceiver and derives various positions, materials and edges of the target area.

In the PolSAR imaging system, the polarization scattering matrix **S** is a convenient way to represent the scattering characteristics of a single pixel, which contains all the polarization information of the target [61]. Vectorizing **S** to obtain the normalized covariance matrix **C** [6, 7, 27]:

$$\langle \mathbf{C} \rangle = \left\langle \mathbf{k}\mathbf{k}^{\dagger} \right\rangle, \tag{6}$$

$$\mathbf{k} = \frac{1}{\sqrt{2}} \left[S_{\mathrm{HH}} + S_{\mathrm{VV}}, S_{\mathrm{HH}} - S_{\mathrm{VV}}, 2S_{\mathrm{HV}} \right]^{T}, \tag{7}$$

where S_{VV}, S_{HV} and S_{HH} correspond to the information when the transmission and reception are vertical polarization and horizontal polarization respectively, and **k** and $\mathbf{k}^{\dagger}$ are the polarized scattering vector using the Pauli bases and its conjugate transpose. The PolSAR imaging is generally performed on **C**. Specifically, decomposing **C** into eigenvectors to obtain several parameters (polarization entropy, anisotropy, Wishart distance and etc.), applying some models to classify and edge detect PolSAR image pixels, and finally form 2-D PolSAR images [11, 14, 19, 28, 47]. In this paper, we utilize the principle similar to PolSAR imaging to identify the edges of different materials based on COTS WiFi devices, but we do not use matrix **C** to achieve this.

3 OVERVIEW

3.1 Problem Statement

As shown in Fig. 6, the goal of *Wi-Painter* is to allow orthogonally polarized (*e.g.* , horizontally and vertically polarized) commercial WiFi signals (*e.g.* , $5GHz/40MHz$) to detect the location, materials and edges of the surrounding smooth-surfaced object, which typically include but not limited to desk, refrigerator, sheet metal, and wall. Note that in our research, we construct object-specific features based on quasi-specular signals at multiple incident angles, where quasi-specular occurs when the signal wavelength is larger than the object surface roughness [3, 39, 54]. To this end, we need to move the WiFi transceiver to build different WiFi rays for ensuring that object in space can be scanned from different angles. Specifically, *Wi-Painter* takes *channel*

state information (CSI) measurements from the receiver during movement of WiFi transceiver as input, and then derive the object's location, materials, and edges.

3.2 *Wi-Painter*'s Architecture

In this paper, the positions and orientations of the transmitting and receiving antennas are precisely known, and these antennas are basically at the same height. This makes each WiFi ray horizontal, which is feasible since our scheme generalizes easily from low to high dimensions.

Material localization and reflected power extraction (§5). We represent the multipath channel by parameters such as AoD, AoA, the attenuation, and path delay for each path, and iteratively estimate these parameters of each mirror point by following the approach of mD-track [59]. Then we move the transceiver to refine the path parameters for achieving centimeter-level localization accuracy and extract accurate reflected power. After this process, several mirror points are combined into a reflected region.

Basic model for material identification and edge detection (§4). We measure the power ratios of orthogonally polarized signals at multiple incident angles, which can identify different materials without frequency-dependent features. After this process, a plurality of adjacent reflective regions under different incident angles are combined into an image pixel. Then we measure multiple image pixels in 2D and identify their materials, and detect edges based on material identification, thus forming a 2D image.

Material edge refinement and strong speckle removal (§6). we build Gaussian shaped filter to judge whether it is an edge or not according to the difference between the two sides of the central pixel, and fit successive edge pixels of the same material to outline the accurate material edge.

4 BASIC MODEL FOR MATERIAL IDENTIFICATION AND EDGE DETECTION

In this section, we introduce our basic model for fine-grained material identification and edge detection based on orthogonally polarized commercial WiFi signals.

4.1 Estimation of the Complex Permittivity from Power Ratio for Different Incident Angles

We first briefly introduce how the traditional amplitude-phase based polarimetry method estimates the complex permittivity of the object surface. Then, we illustrate the problem of the phase imprecision of COTS WiFi devices, and verify the fact that materials can be characterized using only the power ratio of orthogonally polarized signals at multiple incident angles.

Applying Euler's formula $e^{j\Psi} = \cos\Psi + j\sin\Psi$ into Equ. 5, the real and imaginary parts of the complex permittivity can be obtained as follows:

$$\text{Re}\,\varepsilon = \left[1 + 4|\mathcal{P}|\frac{\left(1 + |\mathcal{P}|^2\right)\cos\Psi - 2|\mathcal{P}|}{\left(1 - 2|\mathcal{P}|\cos\Psi + |\mathcal{P}|^2\right)^2}\sin^2\alpha\right]\tan^2\alpha,$$

$$\text{Im}\,\varepsilon = 4|\mathcal{P}|\frac{\left(1 - |\mathcal{P}|^2\right)\sin\Psi}{\left(1 - 2|\mathcal{P}|\cos\Psi + |\mathcal{P}|^2\right)^2}\sin^2\alpha\tan^2\alpha,$$

(8)

where $|\mathcal{P}|$ and Ψ are the power ratio and phase difference of the vertically polarized and horizontally polarized signals reflected by the object material, and α is the incident angle. In this way, given that the incident angle α is known, we can transmit vertically polarized and horizontally polarized WiFi signals of equal power, and receive them at the receiving end using vertically polarized and horizontally polarized antennas, respectively. Then the power ratio and phase difference of the orthogonally polarized channels can be obtained to get the complex permittivity of the material.

However, the phase difference of the orthogonally polarized channels is difficult to obtain accurately, mainly because the phase error introduced by SFO and ToF in WiFi NIC [58, 62], and the propagation path of orthogonally
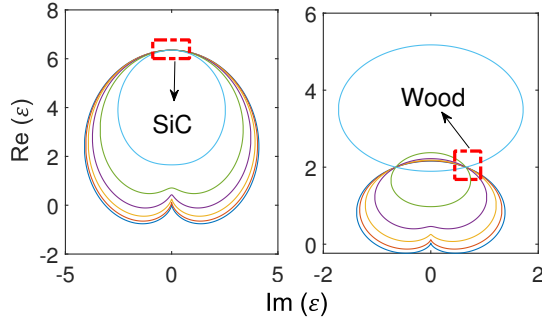
Fig. 7. Using the power ratio of the reflected orthogonally polarized signals at different incident angles, the complex permittivity ε of the material can be approximated.
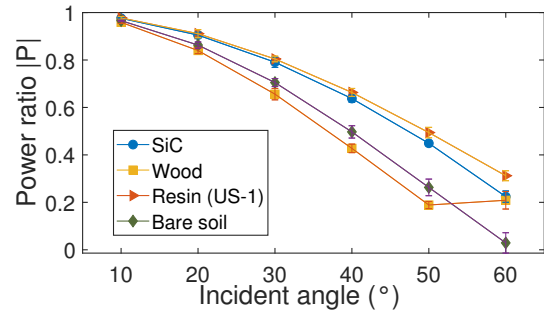
Fig. 8. The power ratios of orthogonally polarized signals reflected by different materials are different at some incident angles.
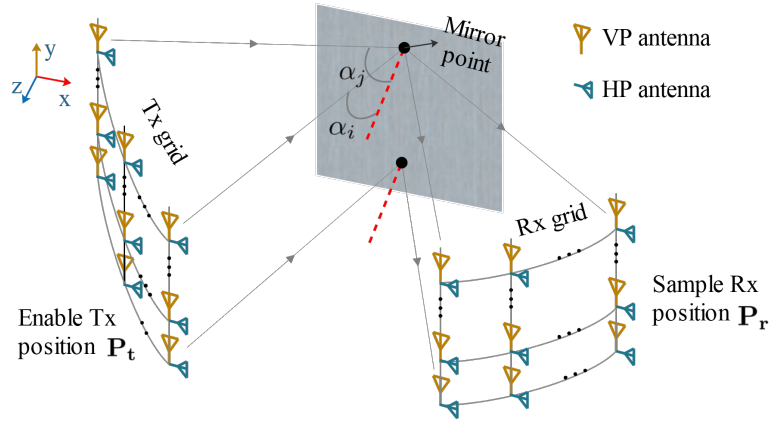

Fig. 9. We construct the Tx antenna grid and the Rx antenna grid around the target material, and when Tx and Rx are at certain position (P_t^k, P_r^k), the condition of certain incident angle α^k to certain mirror point k can be formed.

polarized signals cannot be guaranteed to be consistent. This leads to a large error in the complex permittivity determined based on the power-phase method. On the other hand, the power ratio can generally be obtained accurately, but the complex permittivity cannot be measured only from the power ratio. Our observation is that the real part Re ε and imaginary part Im ε of the complex permittivity is also closely related to the incident angle α, as described in Equ. 8. So can we get the complex permittivity of the material through the power ratio $\{|\mathcal{P}^1|, |\mathcal{P}^2|, \cdots, |\mathcal{P}^k|\}$ at different incident angles $\{\alpha^1, \alpha^2, \cdots, \alpha^k\}$?

In order to verify this, we obtain the power ratios of four different materials when the incident angles are $[10°, 60°]$ with interval is $10°$ based on simulation data. Then, for each incident angle's power ratio $(\alpha^k, |\mathcal{P}^k|)$, we traverse the phase difference in the range $[0, 360°]$ to calculate the real part Re $\varepsilon(\Psi)$ and imaginary part Im $\varepsilon(\Psi)$ of the complex permittivity according to Equ. 8, where Ψ is the phase difference. Finally, for the set $\{\cdots, (\text{Re }\varepsilon(\Psi_i), \text{Im }\varepsilon(\Psi_i)), \cdots, (\text{Re }\varepsilon(\Psi_j), \text{Im }\varepsilon(\Psi_j)), \cdots\}$ under each power ratio $|\mathcal{P}^k|$, we can fit a closed curve, so multiple sets obtained under multiple power ratios fit several curves, as shown in Fig. 7. Obviously, the several curves fitted by one object approximates to one point, which corresponds to the complex permittivity ε of the
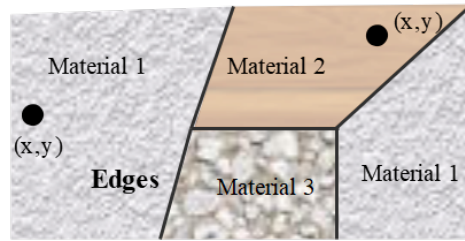
Fig. 10. We scan each mirror point on 2D and identify the material type according to the extracted orthogonal polarization signal ratio of multiple incident angles, and then characterize the edges of different materials based on the material identification.

object. Therefore, the complex permittivity of the object can be accurately measured based on the power ratio at different incident angles.

Furthermore, in many scenarios (*e.g.* , narrow aisles and corners) we may not be able to obtain power ratios in the range $[0, 90°]$, so it is not always possible to fit the complex permittivity. However, the power ratios of different materials at different angles of incident are always different. Therefore, for the convenience of calculation, we only use $(\alpha^k, |\mathcal{P}^k|)$ as the feature representing the complex permittivity of the object material:

$$\mathbf{g} = \left[|\mathcal{P}^1|, |\mathcal{P}^2|, \cdots, |\mathcal{P}^M| \right], \tag{9}$$

where M is the number of incident angles. As shown in Fig. 8, we perform multiple simulations, and the results show that the power ratios of orthogonally polarized signals by different materials are different at some incident angles. So far, we have built a material feature that only depends on the power ratios and incident angles, which is stable for commercial WiFi devices.

4.2 Obtaining Power Ratios for a Wide Range of Incident Angles

There are two important prerequisites for characterizing materials using the power ratio of orthogonally polarized signals at multiple incident angles. The first premise is that the range of incident angles needs to be wide enough. Note that there is little difference in the power ratios of the orthogonally polarized signals reflected by different materials at small incident angles, while the difference may be more pronounced at larger incident angles, as shown in Fig. 8. The second premise is that the orthogonally polarized signal must be reflected by the material at the same position. This is especially critical in our system, where we require signals at different incident angles to be reflected by quasi-specular reflected mirror points.

In order to satisfy these two premises, our method is to construct the Tx antenna grid and the Rx antenna grid around the object material, as shown in Fig. 9, the positions $(\mathbf{P}_t, \mathbf{P}_r)$ of the transceiver are known in our system. We then estimate the position (x^k, y^k, z^k) and orientation θ^k of reflected mirror point, and obtain the incident angle α^k and reflected power ratio $|\mathcal{P}^k|$ of orthogonally polarized signals. The detailed process is described in Section 5.

4.3 Edge Detection Based on Material Identification

In order to detect the edges of different materials, we abstract the target object into a 2D image composed of multiple mirror points. Then we construct Tx grid and Rx grid around each mirror point to calculate the orthogonal polarization power ratios under several incident angles, and use these power ratios to estimate the material corresponding to the mirror point (x, y). As shown in Fig. 10, a 2D image should be formed in the end,

where different colors represent different material types. Then, we can draw the edges of different materials on the basis of material identification, as shown in the black line in Fig. 10.

However, there are two problems with edge detection based on material identification, as shown in Fig. 12. The first is that the power ratio of the orthogonally polarized signals acquired at the edge of the material does not belong to any material on both sides, or the power ratio calculation error is large in the same material, which leads to material identification errors. We call this phenomenon is strong speckle. The other is that the mirror point reflected by WiFi signal is actually an area of about half a wavelength, and the estimation error of the position of the mirror point may be large, which leads to inaccurate outline of the edges. We give specific solutions for these two problems in Section 6.

5 MATERIAL LOCALIZATION AND REFLECTED POWER EXTRACTION

It can be known from Section 4 that fine-grained material identification and edge detection require accurate acquisition of four parameters: the coordinate (x^k, y^k, z^k) and orientation θ^k of each mirror point, the incident angle α^k and reflected power ratio $|\mathcal{P}^k|$ of orthogonally polarized signals. In this section, we then present our scheme to accurately obtain these parameters based only on the locations of the WiFi transceiver and the measured CSIs.

Assuming that the positions of the transceiver in space are known to be (x_t^k, y_t^k, z_t^k) and (x_r^k, y_r^k, z_r^k) when Tx and Rx are in positions P_t^k and P_r^k, as shown in Fig. 9. Note that when moving the transceiver or the object material to construct Tx grid and Rx grid, we always keep the Tx and Rx at the same height. Although Tx and Rx are not set at the same height to construct the two complete antenna grids, setting them at the same height makes the system easier to deploy, and this will not affect the normal operation of the model in Section 4. Next, we take Tx and Rx at height $y_t^k = y_r^k = y^k$ as the example to illustrate the details of our scheme.

5.1 Basic Model of Separating Signal Paths

Considering that surfaces appear quasi-specular at lower frequencies such as WiFi [39], we are actually measuring each mirror point. In this paper, we use a method similar to mD-track [59] to obtain the signal reflected from the mirror point. For a multipath channel, each path is represented by the AoD φ, the AoA Φ, the attenuation γ and the path delay τ. The multipath channel can be expressed as:

$$\mathbf{H} = \sum_{l=1}^{L} H\left(\varphi_l, \Phi_l, \gamma_l, \tau_l\right) + W, \tag{10}$$

where W is the Gaussian noise matrix.

To get the locations and orientations of multiple mirror points, we need to extract the path parameters of the reflection path from the multipath channel. We follow the approach of mD-track [59] to achieve this. Specifically, we first reconstruct the strongest path and its parameters, then we subtract it to get the channel residual for iterative estimation of path parameters, which can isolate weaker reflection paths [4]. We get the path parameters:

$$(\hat{\varphi}, \hat{\Phi}, \hat{\tau}) = \underset{\varphi, \Phi, \gamma, \tau}{\arg\max} |z\left(\varphi, \Phi, \tau\right)|, \tag{11}$$

$$\hat{\gamma} = \frac{z\left(\hat{\varphi}, \hat{\Phi}, \hat{\tau}\right)}{N_{ant} \cdot T_s}, \tag{12}$$

where $z\left(\varphi, \Phi, \tau\right)$ is a multidimensional estimator designed to maximize the power of the received channel over a set of possible path parameters, N_{ant} is the number of total antennas and T_s is the signal duration.
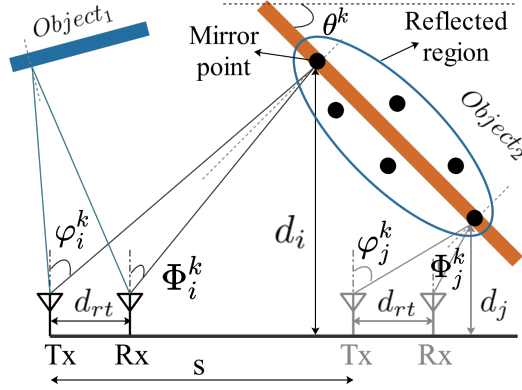
Fig. 11. The position of each mirror point of the target material is estimated based on the multipath model, and the multipath parameters are refined using several consecutive mirror points (a reflected region).

It should be specially stated that although the algorithm of mD-Track for estimating path parameters also needs to use the phase information of multiple antennas, it is different from the phase used by the traditional amplitude-phase method using orthogonally polarized signals to estimate the complex permittivity of material. Specifically, mD-Track estimates parameters such as AoA and attenuation by using multi-antenna phase differences, and removes additional phase errors introduced by SFO through methods such as conjugate multiplication. However, the traditional magnitude-phase method needs to directly use the precise absolute phase measurements of two different polarization directions, and requires that the reflected electromagnetic waves of the two different polarization directions come from the same propagation path. Therefore, compared with the latter, the phase information of WiFi signals with two different polarization directions is enough to estimate the path parameters respectively.

5.2 Estimation of Mirror Points' Parameters Based on Multipath Channel

Traditionally, based on the iterated path parameters and the geometric principle of quasi-specular reflection, we get the orientation $\hat{\theta}^k$ and incident angle $\hat{\alpha}^k$ of the mirror point at (P_t^k, P_r^k) as follows:

$$\hat{\alpha}^k = \frac{\hat{\varphi}^k - \hat{\Phi}^k}{2},$$ (13)

$$\hat{\theta}^k = \hat{\theta}_{tr\_mp}^k + \theta_{tx\_rx}^k = \frac{\hat{\varphi}^k + \hat{\Phi}^k}{2} + \arctan\frac{z_r^k - z_t^k}{x_r^k - x_t^k},$$ (14)

where $\hat{\theta}_{tr\_mp}^k$ is the relative angle between the mirror point and the transceiver, and $\hat{\theta}_{tx\_rx}^k$ is the orientation of the transceiver, as shown in Fig. 11. And the power ratio of orthogonally polarized signals is:

$$|\hat{\mathcal{P}}^k| = \frac{|\hat{\gamma}_{vp}^k|^2}{|\hat{\gamma}_{hp}^k|^2},$$ (15)

where $\hat{\gamma}_{vp}$ and $\hat{\gamma}_{hp}$ represent the attenuation factors of vertical polarization and horizontal polarization signal propagation respectively, and they are different because of the existence of the complex permittivity, as described in Section 2.

Although we assume that the resolution of τ can distinguish signals from different paths in this paper (e.g. , at 80 MHz bandwidth, paths with a difference of 3.75 m can be distinguished), there are still large fluctuations in the estimated value of τ. Therefore, we only use the estimated AoA and AoD (i.e. , φ and Φ) to locate the mirror point. Specifically, we first estimate AoA and AoD separately, and then use triangulation method to estimate the position of the mirror point.

5.3 Parameters Refinement of the Image Pixel in Mobile Settings

In particular, to improve accuracy of edge detection, we need to accurately estimate each mirror point's position (centimeter level or even better), orientation, incident angle, and power ratio. To achieve this, we build the equal-complementary angle model by moving the transceivers or the object material to take advantage of the geometry, thereby enhancing multipath separation. Considering some potential scenarios such as assembly line testing of material quality in automated factories and airport security checks, such settings are reasonable. As shown in Fig. 11, we observe that according to the principle of specular reflection, when the transceiver or the object material is moved along a straight line for a small distance s (e.g. , 2 cm), the mirror point moves a distance of L. We consider that within this distance, the orientation of the reflector remains unchanged. According to the geometric relationship between AoA and AoD ($\hat{\varphi}_i + \hat{\Phi}_i = \hat{\varphi}_{i+1} + \hat{\Phi}_{i+1}, i = 1, 2, \cdots$), we can get angles ($\hat{\varphi}'^k, \hat{\Phi}'^k$) of the reflection region as follows:

$$(\hat{\varphi}'^k, \hat{\Phi}'^k) = \frac{1}{N^k} \sum_{i=1}^{N^k} \underset{\hat{\varphi}^k, \hat{\Phi}^k}{\arg\min} ||(\hat{\varphi}_i^k + \hat{\Phi}_i^k) - (\hat{\varphi}_j^k + \hat{\Phi}_j^k)||^2, \tag{16}$$

where N^k is the number of mirror points measured by the transceiver. Then we put ($\hat{\varphi}'^k, \hat{\Phi}'^k$) into Equ. 13 and Equ. 14 to obtain $\hat{\theta}'^k$. And the ToF $\hat{\tau}'^k$ is:

$$\hat{\tau}'^k = \frac{\hat{d}^k (\sec \hat{\varphi}'^k + \sec \hat{\Phi}'^k)}{c} = \frac{d_{rt}^k (\sec \hat{\varphi}'^k + \sec \hat{\Phi}'^k)}{(\tan \hat{\varphi}'^k - \tan \hat{\Phi}'^k) \cdot c}, \tag{17}$$

where d_{rt}^k is the distance from Tx to Rx and c is the speed of light. Then we put ($\hat{\varphi}'^k, \hat{\Phi}'^k, \hat{\tau}'^k$) into Equ. 12 and Equ. 15 to obtain $|\hat{\mathcal{P}}'^k|$. It is worth noting that several mirror points of orthogonally polarized signals are combined into a reflected region, and multiple reflected regions with different incident angles form an image pixel, and the image pixel center is the centroid of these reflected regions.

6 MATERIAL EDGE REFINEMENT AND STRONG SPECKLE REMOVAL

6.1 Gaussian Shaped Filter to Remove Strong Speckle

Some strong speckle in the image may reduce the detection accuracy of materials and edges, as shown in Fig. 12. We build the Gaussian shaped filter and apply it to all image pixels to handle this problem, and get the weight of the pixel (x, y):

$$W(x, y) = \frac{1}{\sqrt{2\pi}\sigma_x \sqrt{2\pi}\sigma_y} \exp\left(-\left(\frac{x^2}{2\sigma_x^2} + \frac{y^2}{2\sigma_y^2}\right)\right), \tag{18}$$
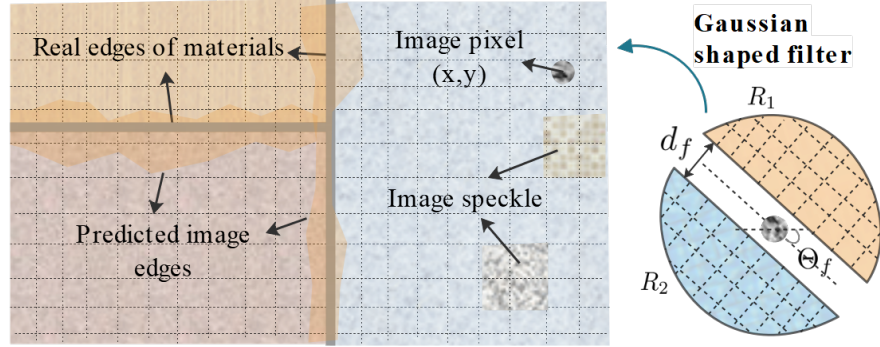
Fig. 12. We use Gaussian shaped filter to remove strong speckle in 2D image constructed based on material identification, and then fit the predicted image edges to outline smooth and accurate real material edges.

where σ_x and σ_y are the dimensions of the filter window. We determine the most material types T_1, T_2 on both sides, and define the pixels on both sides as follows:

$$C(x, y) = \begin{cases} 0, & T(x, y) = T_1 = T_2 \\ 1, & T(x, y) \neq T_1 \neq T_2, \\ 2, & T(x, y) = T_1 \neq T_2. \end{cases} \tag{19}$$

Then we get the local weighted function on both sides of the center pixel respectively:

$$\mathbf{Z} = \frac{\sum_{(x,y)} W(x, y) C(x, y)}{\sum_{(x,y)} W(x, y)}. \tag{20}$$

Obviously, in this process, the closer to the image pixel center, the higher the weight. Therefore, based on the Gaussian shaped filter, we can obtain the more accurate difference matrix on both sides of the center pixel.

Next, we compute the sum of the differences on either side of the center pixel:

$$D(\mathbf{Z_1}, \mathbf{Z_2}) = ||\mathbf{Z_1}|| + ||\mathbf{Z_2}||. \tag{21}$$

Furthermore, we compute Gaussian weight $W(x, y)$ and the difference matrix Z for different orientation Θ, and take its maximum value and corresponding orientation:

$$\begin{aligned} D_{max} &= \max \ D(\mathbf{Z_1}, \mathbf{Z_2}, \Theta) \\ \Theta_{max} &= \arg \max_{\Theta} D(\mathbf{Z_1}, \mathbf{Z_2}, \Theta). \end{aligned} \tag{22}$$

By comparing D_{max} with our preset threshold D_{thre}, it is judged whether the central pixel is an edge pixel. Finally, we set the discriminated central pixel as the most material type on both sides, and repeat the above process for all pixels. Note that in this paper, we set the window size to $(\frac{3}{2\sqrt{\pi}}, \frac{5}{2\sqrt{\pi}})$, and set $D_{thre} = 1.2$, these are experience values.

6.2 Curve Fitting to Refine Material Edges

Estimating mirror point locations using WiFi signals may result in inaccurate edge contours, as shown in the predicted image edges in Fig. 12. In order to improve the edge detection accuracy of different materials, on the

basis of removing strong speckle based on Gaussian shaped filter, we fit successive edge pixels of the same material to outline smooth and accurate material edges, as shown in the real edges of materials in Fig. 12. In particular, the edges of different materials in our deployment are linear, so we use the linear fitting method in this paper. Please note that this paper does not discuss too much about the method of material edge fitting, which can be one of future work.
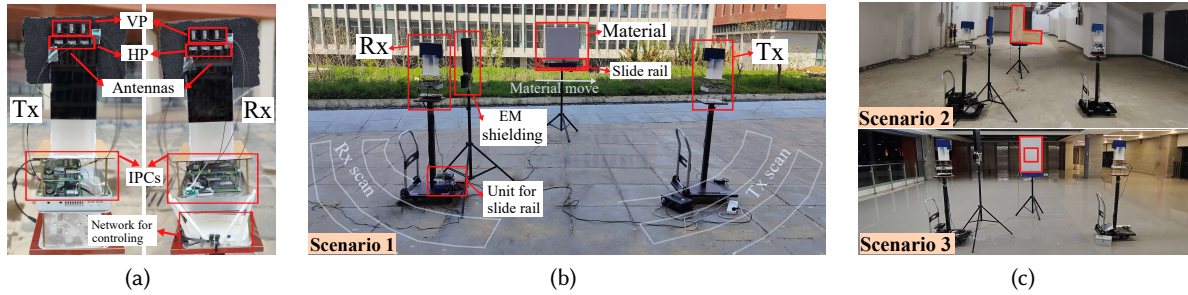

Fig. 13. *Experimental implementation:* (a) Design of orthogonal polarization antenna array for Tx and Rx. (b) Radiation pattern of omnidirectional antenna. (c) Effect of directivity on received power.
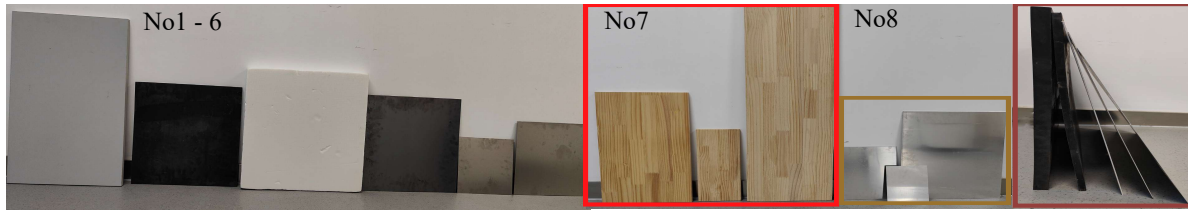

Fig. 14. Boards with different materials (No1 - 8: particle, rubber, plastic, iron, titanium, steel, solid wood, aluminum), different sizes (solid wood: $40 \times 20cm$, $40 \times 60cm$, $40 \times 120cm$; aluminum: $20 \times 20cm$, $30 \times 30cm$, $40 \times 40cm$) and different thicknesses (rubber: 15 mm; 30 mm, aluminum: 3 mm, 2 mm, 1 mm).

7 PLATFORM IMPLEMENTATION

Hardware implementation. As shown in Fig. 13a, we build *Wi-Painter* based on four industrial personal computers (IPCs) with WiFi NICs IWL5300, and with Intel Core i7-5550U CPU and 8 GB RAM, running on Ubuntu 14.04 LTS. Two of them are used as Tx, and the others are used as Rx. Each NIC is connected to three antennas to deal with multipath. In order to accurately measure the power ratio of orthogonal polarizing signal, we use 3×4 linear polarization antennas with the same parameters to construct antenna arrays of vertical polarization (VP) and horizontal polarization (HP). In each set of antenna arrays, the antenna separation is half-wavelength to more accurately extract path parameters. In particular, the VP antenna and the HP antenna are set in the same vertical direction, and the interval is slightly greater than a quarter of wave (avoiding the antenna interval is too close to the electric field coupling, and the interval is too far to reduce the edge detection accuracy). Then we place TX and RX on two easy-to-move small hand carts, as shown in Fig. 13b. In addition, we use electromagnetic (EM) shielding LoS signals and reflected signals behind the antenna arrays because the estimated range of AoA is $[-90\,^{\circ}, 90\,^{\circ}]$. For convenience, we place the materials on the slide rail and move them to detect the materials
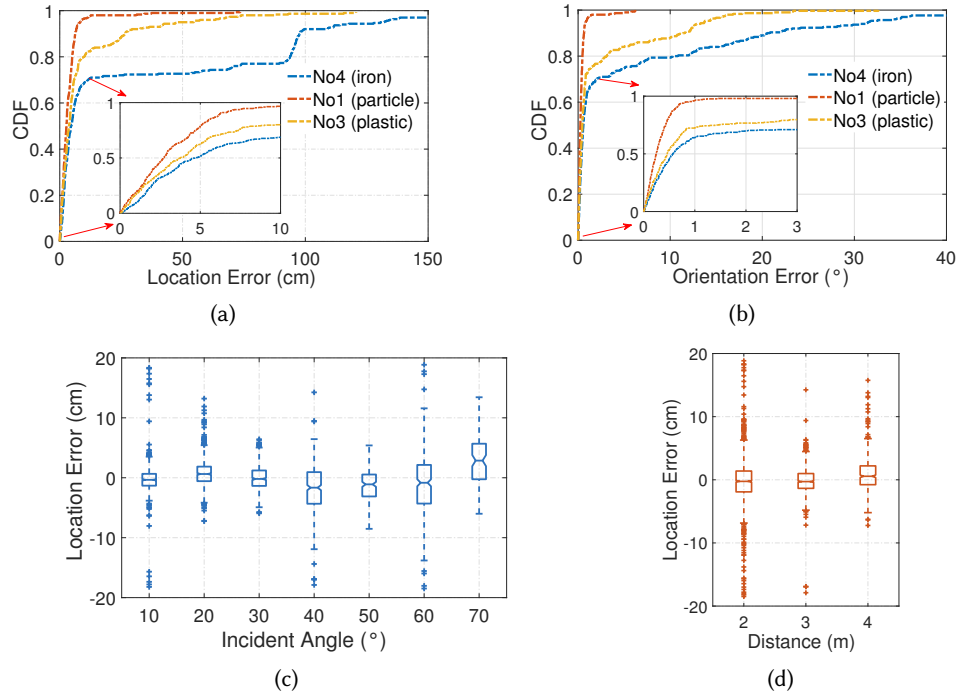
Fig. 15. *Accuracy of object location and orientation:* (a) Location accuracy of three different object materials. (b) Orientation accuracy of three different object materials. (c) The impact of different incident angles on object location accuracy. (d) The impact of different distances on object location accuracy.

and edges. Such setting is reasonable in scenarios such as automated factory assembly lines and airport security checks.

Software and data collection. We install *Linux 802.11 CSI Tool* on each IPC and keep TX and RX work in the injection and monitor mode separately to collect CSIs. We keep HP and VP signals work separately at 64 channel (*i.e.*, $5.32GHz/40MHz$) and 161 channel (*i.e.*, $5.805GHz/40MHz$) to avoid interference from frequency overlap. It is worth noting that work in different channels is feasible, because the complex permittivity of solid almost does not change with frequency, as described in Section 1. In order to collect data under different incident angles (*e.g.*, $10°, 20°, \cdots$), we move TX and RX to the marked positions and orientations to achieve TX scan and RX scan. Then, we move the slide rail at a specific distance (*e.g.*, 2 cm), collect CSIs from HP and VP channels, and repeat this process under each incident angle and each height.

8 EVALUATION

8.1 Experimental Setup

We evaluate *Wi-Painter*'s performance in real world deployment. To this end, we deploy *Wi-Painter* in three different scenarios, including outdoor and indoor environments, as shown in Fig. 13b and Fig. 13c. As shown in Fig. 14, we place 16 boards in these scenarios to identify their materials, which contain 8 different kinds of materials (particle, rubber, plastic, iron, titanium, steel, solid wood, aluminum) and the same kind of materials with different sizes and different thicknesses. It is worth noting that the surfaces of titanium and steel look very

similar. Then we combine several materials of different or same types into one object, and place the combined object in different directions so that the edges of the materials have different orientations, in particular, we concatenate the word "LOVE", as shown in Fig. 17. Next, we evaluate our proposed models and techniques in terms of the accuracy of object material location and orientation, the accuracy of identifying various materials and the accuracy of detecting multiple material edges in detail.

8.2 Accuracy of Object Location and Orientation

In order to verify the baseline accuracy in estimating object location and orientation, we deploy our system in Scenario 1 and select three boards of different materials (*i.e.*, No1 particle, No3 plastic, No4 iron) for testing. As shown in Fig. 13b, we first precisely fix the position, orientation and height of the slide rail, and then fix the three boards on the slide rail respectively. We place the Tx and Rx at the marked positions and orientations, specifically, we make the incident angles $10°$, $20°$, $30°$, $40°$, $50°$, $60°$, $70°$ respectively. We move the slide rail 10 times horizontally with 2 mm interval at each position and collect CSIs during 10 s, 10 times for each board. We use the center coordinates of the reflected regions of the HP and VP channels estimated at 7 different incident angles as the location of the object material (more specifically, each 2D image pixel), and use the mean values of the estimated AoA and AoD at 7 different incident angles to calculate the orientation of the object material. As shown in Fig. 15a and Fig. 15b, for different objects, the median error of location is less than 5 cm, and the median error of orientation is less than one degree.

In addition, we validate the location estimation accuracy at different incident angles, which is necessary because *Wi-Painter* uses the power ratio of the orthogonally polarized signals at multiple incident angles as the feature for identifying materials and detecting edges. We calculate the center coordinates of the reflected regions of the HP and VP channels at 7 different incident angles respectively. The results are shown in Fig. 15c, and it can be seen that the average location error is less than 6 cm. Furthermore, WiFi signals travel different distances. We respectively estimate the accuracy of the location when the distance from the transceiver to the target material is 2 m, 3 m, and 4 m. As shown in Fig. 15d, the average location error is less than 3 cm at different distances.

8.3 Accuracy of Identifying Various Materials

To evaluate the performance of material identification based on the power ratio of orthogonally polarized signals at multiple incident angles, we placed 16 boards as shown in Fig. 14 in Scenario 1 for testing. Here, we collect CSIs for each board for 20 s at incident angles of $10°$, $20°$, $30°$, $40°$ to calculate the power ratio, and then identify different materials based on the four power ratios. The data of each board at each incident angle is divided into 100 sets. Our material identification model does not rely on the complex features of the raw CSIs, so we can use simple classification methods. Specifically, we use *k-Nearest Neighbor* (KNN) to classify 8 different materials, where the training set and test set each account for 50% of the data (*i.e.*, 50 sets of data are used for training, 50 sets data for prediction). We set k of KNN to 10 for 1000 repeated experiments and use Euclidean distance as the distance metric of KNN. As shown in Fig. 16a, the average accuracy of material classification is 96%. In particular, for No. 5 (titanium) and No. 6 (steel) as shown in Fig. 14, which look very similar on the surface, *Wi-Painter* can still accurately identify them, which is very challenging for computer vision-based solutions.

It is worth noting that since KNN does not require an explicit training process, we can easily add new materials. In particular, we can build a material database based on existing materials. When identifying an unknown material, we set a threshold to determine whether the unknown material belongs to the original material database. When an unknown material is detected as an original material, we add it under the original material. When the unknown material is detected as not being in the original material, we add a new material and add it to the new material. However, since there is no prior knowledge of the material, we only classify it as a new material and
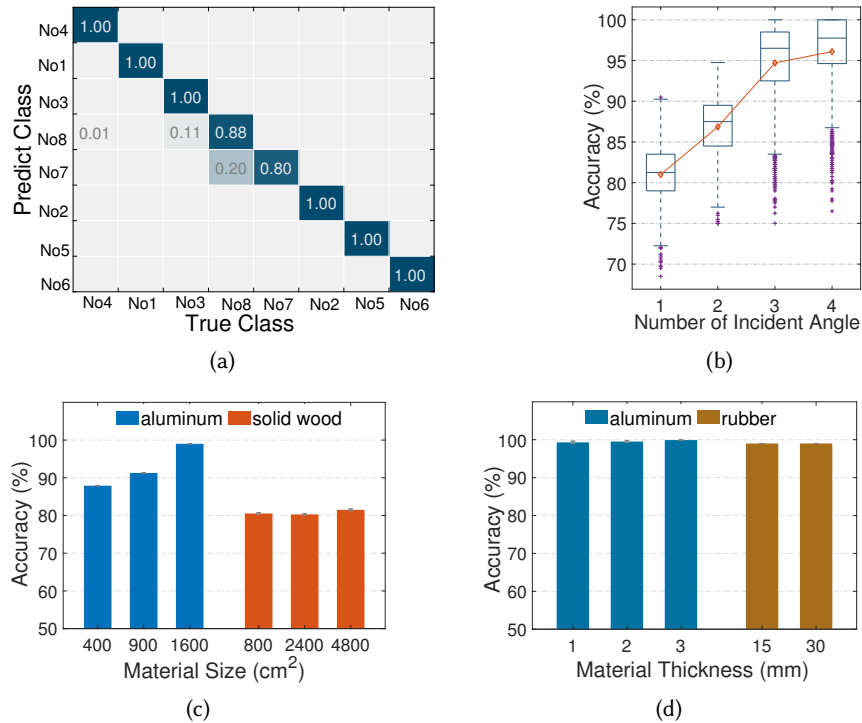
Fig. 16. *Accuracy of identifying various materials:* (a) Confusion matrix for identifying 8 different types of materials based on power ratios at 4 incident angles. (b) The impact of the number of power ratios with different incident angles on material identification accuracy. (c) The impact of size on material identification accuracy. (d) The impact of thickness on material identification accuracy.

cannot accurately obtain its material category (*e.g.*, which type of wood or metal). We consider this as one of our future work.

The accuracy of material identification based on the power ratio of orthogonally polarized signals at multiple incident angles is directly affected by the number of power ratios. We use the power ratios with 1, 2, 3, and 4 incident angles to identify material types for analyzing this effect in detail. Specifically, there are 4 situations for 1 incident angle, *i.e.*, $10°, 20°, 30°, 40°$; there are 6 situations for 2 incident angles, *i.e.*, pairwise combinations of 4 incident angles; there are 4 situations for 3 incident angles, and one situation for 4 incident angles. As shown in Fig. 16b, the average accuracy improves with the number of power ratios at different incident angles.

In addition, the same material type has different sizes and thicknesses. We identify three different sizes of aluminum and solid wood respectively, with an average accuracy of 92% and 81%, and the results are shown in Fig. 16c. We also identify three different thicknesses of aluminum and two different thicknesses of rubber, and the results are shown in Fig. 16d, with an average accuracy of 99% and 99%.

8.4 Accuracy of Detecting Multiple Material Edges

Before evaluating these, in order to better visualize the material edges, we define the 8 materials used and background (*i.e.*, no target) as 9 different colors as shown in Fig. 18.
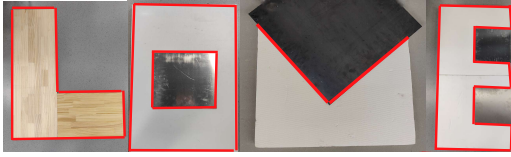
Fig. 17. We concatenate the word "LOVE" for material edge detection, which includes edges made of the same material, edges made of different materials, and edges with different orientations.
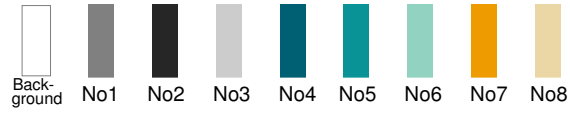

Fig. 18. We define the 8 materials used and background (*i.e.*, no target) as 9 different colors.
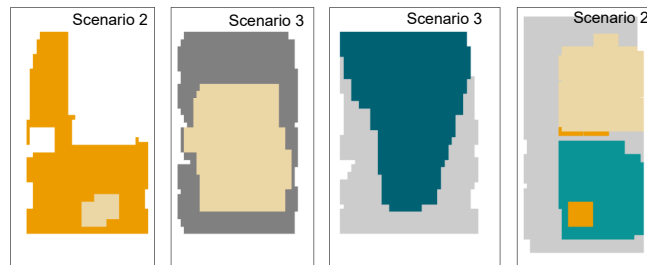

Fig. 19. Simple imaging results based only on localization and material identification, in two different scenarios.

Sample imaging results. In Scenario 2 and Scenario 3 , we put the concatenated word "LOVE" by the same material or different materials as shown in Fig. 17 to further identify the material and detect the edges of the materials. Likewise, we collect CSI data at incident angles of $10°$, $20°$, $30°$, $40°$, respectively. We fix the four spliced boards on the slide rails in turn, move the boards horizontally 2 cm each time and collect the CSI during the period, then move the boards vertically 2 cm, and repeat this process. In particular, we move four letters 50 cm horizontally. However, for the letters "L", "O", and "V", we move 50 cm vertically, and for the letter "E", we move 100 cm vertically.

We calculate the position of each pixel and the power ratios of the orthogonally polarized signals from the collected CSI data and classify them. Then, based on the localization and material classification results, we map the image. The result is shown in Fig. 19. It can be seen that the contours of the four letters can basically be described very well. However, there are some strong speckles inside the same material. What's more, this simple imaging is imprecise in detecting the edges of different materials, suggesting that the refinement is necessary.

Refined imaging results. In order to obtain refined material identification and edge imaging results, we add Gaussian shaped filter to each pixel on the basis of simple imaging results. In particular, we set the window size to $(\frac{3}{2\sqrt{\pi}}, \frac{5}{2\sqrt{\pi}})$, and set $D_{thre} = 1.2$, note that these are experience values. The non-edge pixels are then reset to the material type that occurs most frequently around them. In addition, we linearly fit the edge pixel coordinates using least squares to smooth them. The result is shown in Fig. 20, where the red lines are the edges of different materials. It can be seen that the strong speckles in the original image are filtered out, and the edges are clearer.

Impact of different environments. Materials may be placed in different environments. In order to verify the robustness of *Wi-Painter* to the environment, we place the spliced four letters in two different scenarios as shown in Fig. 13c for testing. Specifically, the letters "L" and "E" are placed in Scenario 2, and the letters "O" and "V" are
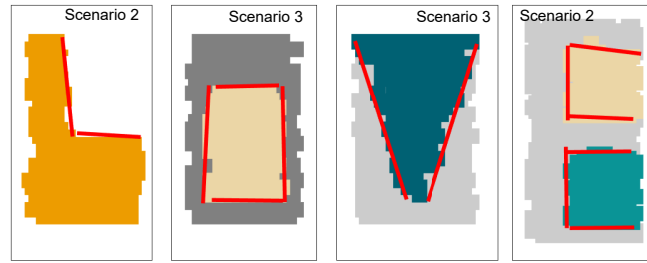
Fig. 20. Refined imaging results after using Gaussian shaped filter and edge fitting on the basis of simple imaging, where the red lines are the edges of different materials, in two different scenarios.

placed in Scenario 3. Then we combine the four letters together for material recognition and edge detection. As can be seen from Fig. 19 and Fig. 20, *Wi-Painter* can cope well with different environments.

9 DISCUSSIONS AND LIMITATIONS

9.1 Potential Real-world Applications and Issues

In particular, we discuss the feasibility of *Wi-Painter* in potential scenarios such as factory automated assembly lines and airport security inspections. Although we have performed experimental verification on a variety of different materials and their combinations, and it is not difficult to automate antenna scanning, data processing and result prediction, there is still room for improvement in the application of these complex real-world scenarios.

Firstly, the environmental interference issue needs to be solved, which is one of the open problems in wireless sensing. Wireless signals, including WiFi, are highly sensitive to the surrounding environments, which is also why we can use them to sense materials. So far we have only evaluated *Wi-Painter* in three relatively simple scenarios, and performance in more complex scenarios awaits further evaluation. In future work, we will focus on solving two situations: how to ensure detection accuracy when there are strong reflection paths and unknown dynamic signals around the detected target and the WiFi transceiver.

Secondly, the ability to detect 3D targets needs to be determined. *Wi-Painter* currently only performs material identification and edge detection on 2D targets, that is, we only consider single-layer target materials. However, there are much more requirements for detecting 3D objects, especially in security inspections where it is common for different objects to be stacked front to back or top to bottom. Since different reflections and transmissions occur at the interface of different media, we plan to build a multiple reflection model in future work to identify multiple layers of different target materials. In addition, we also consider combining our system with other scattering feature-based methods to identify more diverse materials more accurately.

9.2 Setup of the Antennas and Scanning Pattern

In our current implementation, the Tx and RX antenna arrays and their scanning modes are pre-configured, and these settings can be readily automated. However, to be truly deployed in potential scenarios, we need to further consider the impact of deviations these settings may introduce on the performance of *Wi-Painter*.

Firstly, we use four sets of linearly polarized antennas with the same parameters, which are common WiFi antennas that are readily available. However, due to the limitations of the model, deviations in the antenna spacing settings within a single polarization channel and between two polarization channels may seriously affect the effect of material edge detection, but not have an impact on the overall material identification. Specifically, deviations in the antenna settings change the size of each reflective area of the current material, which is not

affected when inside the same material, but may cause more misclassification in areas where different materials are mixed. Although antenna setup deviations affect material edge detection accuracy, we can try to make these deviations in antenna setup be reduced directly during fabrication, which does not add any cost.

Secondly, we use a high-precision slide rail to move the target material and manually move the transceiver to achieve antenna scanning. The deviation of the antenna scanning may be caused by the position deviation of the target material and the transceiver, as well as the deviation of the movement direction, which may also lead to poor detection of the edge of the material. Moreover, when detecting different targets, it may lead to more material misclassification. But similar to antenna setup deviations, we try to reduce such deviations through sophisticated automation implementation and self-calibration. For example, multiple transceivers are used and fixed while only the target material is moved with high precision. We will explore more implementations in future work to account for these deviations without increasing costs.

9.3 Materials are Invisible

We currently perform our systematic evaluation on 16 boards with a total of 8 materials, but these materials are all exposed. However, there are some requirements for detecting materials contained within a common material (*e.g.* , plastic sheet, cloth and etc.), *i.e.* , the materials to be identified are invisible. Furthermore, the material to be identified is located in a carton or suitcase. We think this is a multi-layer material identification problem. In theory, the WiFi signal reflected by the surface of each layer of objects is different, but *Wi-Painter* only considers the reflection of one layer. Therefore, our current solutions still have limitations when it comes to identifying multi-layer materials.

9.4 Solids with Rough Surfaces and Liquids

We have so far only verified a variety of solids with smooth surfaces. It is known that the surface of many materials is rough, but our system can still identify its material type and image it, and this has been applied in the field of remote sensing [29]. However, it is extremely challenging to achieve fine-grained imaging effects because WiFi signals undergo diffuse reflection rather than specular reflection, which makes our model for estimating the position and orientation of each reflection area unusable. Therefore, only larger areas can be identified and imaged. Furthermore, for many liquids, and they are in different containers, liquid type classification based on wireless reflected signals is feasible, but is affected by the type and size of the container [44].

10 RELATED WORK

We briefly review related work with *Wi-Painter* from the following three broad categories:

10.1 WiFi-based Sensing

In recent years, a number of WiFi-based sensing systems have emerged for people tracking [25, 32, 42, 59, 60], health monitoring [34, 36, 50, 68], object imaging [20, 31, 39, 41], material identification [15, 43, 56, 66] and etc. In fact, WiFi signal is becoming a prime candidate for sensing indoor environment due to its ubiquity and can work under NLoS conditions. Generally, WiFi-based sensing systems use CSI as the basic data, which reflects the fine-grained information of signal propagation between WiFi devices and the reflection relative to the human environment. Existing WiFi-based sensing techniques can be divided into model-based such as Fresnel Zone and learning-based methods [63]. Although they have their own advantages and disadvantages, these WiFi-based sensing systems are already sensitive enough, for example, they can construct 3D human mesh [23, 53], as well as monitor breathing/heartbeat [33, 65] and keystrokes [1]. Most relevant to our work are material identification and object imaging.

10.2 Material Identification

Material identification is important for many applications. Some traditionally and commercially employ techniques such as spectroscopy, radar, and X-ray, which, while high in resolution, require specialized equipment that is costly [55, 57]. In recent years, many works have been devoted to the use of RF signals to identify materials, especially liquid identification, including RFID-based [51, 57], UWB-based [9] and WiFi-based [13, 66]. There are also works that use RF signals to identify soil [10, 24]. For example, RSA [69] uses 60 GHz radios to identify the surface material of nearby targets and image their boundaries. RadarCat [64] uses a 60 GHz signal for accurate material classification. TagTag [57] can simultaneously sense multiple targets by utilizing the impedance change of the RFID tag attached to the target. mSense [55] reuses a single commodity mmWave device and uses the reflected signal to extract interpretable and distinguishable features for materials.

LiquID [9] uses UWB signals to attenuate differently when passing through liquids to estimate complex permittivities to identify different liquids. [37] uses UWB signals and machine learning methods to identify a variety of solid materials, but it requires placing different materials on metal sheets and placing directional antennas on the surface of materials to extract material-related features, and it is not suitable for identifying certain solids such as metals. [30] uses the impact of liquid on the amplitude ratio and phase difference of the two receiving antennas of the WiFi device to extract features related to the liquid material. WiMi [13] uses commercial WiFi devices to extract a size-independent feature and identify 10 common liquids well.

In this paper, we are interested in detailed identification of solid materials using WiFi signals. IntuWition [66] utilizes three mutually perpendicular WiFi Rx antennas to identify materials, [46] trains a domain-adaptive model to achieve environment-independent object recognition in luggage using WiFi signals and directional antennas, but they require rich frequency-dependent scattering features. More importantly, these methods cannot fine-grainedly detect the boundaries of multiple materials. Compared with them, *Wi-Painter* utilizes commercial WiFi signals and is able to accurately identify a variety of solid materials with smooth surfaces and outline the edges of multiple materials in a fine-grained manner to achieve imaging.

10.3 Object Imaging

In recent years there has been a lot of work devoted to imaging objects using WiFi signals. In general, much work relies on the standard back-propagation imaging method [20, 49, 67, 70], which utilizes measurements on an Rx grid to form an image of an object by tracing the received signal back to different locations in space, but the The resolution is lower. There are also some works that collect a large amount of data to train a neural network model to image objects [31, 41], but are limited by the size of the training data set. A recent paper proposes a scheme for imaging objects by tracking edges for quasi-specular reflections on smooth objects [39]. In this paper, we are more concerned with the detection of the object's material and its edge, *i.e.*, identifying the type and size of the target material at the same time.

11 CONCLUSION

This paper presents the design and implementation of *Wi-Painter*, to the best of our knowledge, is the first model-driven attempt to perform fine-grained detection of materials and edges using COTS WiFi devices. *Wi-Painter* has two main technical contributions. First, it includes a multi-incident angle model that can characterize the material characteristics of the object surface using only the power ratio of vertically and horizontally polarized WiFi signals, without requiring rich scattering information on the object surface, and does not require WiFi transceivers to perform high-bandwidth scans. Second, unlike previous material identification or imaging systems, it regards the target as two-dimensional pixels, and forms a two-dimensional image simultaneously on the basis of identifying the material type of each pixel. Our real-world evaluations show an average classification accuracy of

93.4% across different material types, sizes, thicknesses, and environments. In addition, *Wi-Painter* can accurately detect the material type and edge of the word "LOVE" spliced with different materials.

ACKNOWLEDGMENTS

REFERENCES

[1] Kamran Ali, Alex X Liu, Wei Wang, and Muhammad Shahzad. 2015. Keystroke recognition using wifi signals. In *Proceedings of the 21st annual international conference on mobile computing and networking*. 90–102.

[2] RMA Azzam. 1986. Relationship between the p and s Fresnel reflection coefficients of an interface independent of angle of incidence. *JOSA A* 3, 7 (1986), 928–929.

[3] HE Bennett and JO119764 Porteus. 1961. Relation between surface roughness and specular reflectance at normal incidence. *JOSA* 51, 2 (1961), 123–129.

[4] Alejandro Blanco, Pablo Jiménez Mateo, Francesco Gringoli, and Joerg Widmer. 2022. Augmenting mmWave localization accuracy through sub-6 GHz on off-the-shelf devices. In *MobiSys'22*. 477–490.

[5] Max Born and Emil Wolf. 2013. *Principles of optics: electromagnetic theory of propagation, interference and diffraction of light*. Elsevier.

[6] Shane R Cloude and Konstantinos P Papathanassiou. 1998. Polarimetric SAR interferometry. *IEEE Transactions on geoscience and remote sensing* 36, 5 (1998), 1551–1565.

[7] Shane R Cloude and Eric Pottier. 1996. A review of target decomposition theorems in radar polarimetry. *IEEE transactions on geoscience and remote sensing* 34, 2 (1996), 498–518.

[8] Ian G Cumming and Frank H Wong. 2005. Digital processing of synthetic aperture radar data. *Artech house* 1, 3 (2005), 108–110.

[9] Ashutosh Dhekne, Mahanth Gowda, Yixuan Zhao, Haitham Hassanieh, and Romit Roy Choudhury. 2018. Liquid: A wireless liquid identifier. In *Proceedings of the 16th annual international conference on mobile systems, applications, and services*. 442–454.

[10] Jian Ding and Ranveer Chandra. 2019. Towards low cost soil sensing using Wi-Fi. In *The 25th Annual International Conference on Mobile Computing and Networking*. 1–16.

[11] Anthony P. Doulgeris, Stian Normann Anfinsen, and TorbjØrn Eltoft. 2008. Classification With a Non-Gaussian Model for PolSAR Data. *IEEE Transactions on Geoscience and Remote Sensing* 46, 10 (2008), 2999–3009. https://doi.org/10.1109/TGRS.2008.923025

[12] GA Emmons and PM Alexander. 1983. *Polarization scattering matrices for polarimetric radar*. Technical Report. ARMY MISSILE COMMAND REDSTONE ARSENAL AL ADVANCED SENSORS DIRECTORATE.

[13] Chao Feng, Jie Xiong, Liqiong Chang, Ju Wang, Xiaojiang Chen, Dingyi Fang, and Zhanyong Tang. 2019. Wimi: Target material identification with commodity wi-fi devices. In *2019 IEEE 39th International Conference on Distributed Computing Systems (ICDCS)*. IEEE, 700–710.

[14] Alejandro C Frery, Renato J Cintra, and Abraao DC Nascimento. 2012. Entropy-based statistical analysis of PolSAR data. *IEEE Transactions on Geoscience and Remote Sensing* 51, 6 (2012), 3733–3743.

[15] Mohamed A Gacem, Amer S Zakaria, Mahmoud H Ismail, Usman Tariq, and Sherif Yehia. 2022. Measurement of Construction Materials Properties Using Wi-Fi and Convolutional Neural Networks. *IEEE Access* 10 (2022), 126100–126116.

[16] David J Griffiths. 2005. Introduction to electrodynamics.

[17] Unsoo Ha, Junshan Leng, Alaa Khaddaj, and Fadel Adib. 2020. Food and liquid sensing in practical environments using rfids. In *Proceedings of the 17th USENIX Symposium on Networked Systems Design and Implementation (NSDI'20)*.

[18] Irena Hajnsek, Thomas Jagdhuber, Helmut Schon, and Konstantinos Panagiotis Papathanassiou. 2009. Potential of Estimating Soil Moisture Under Vegetation Cover by Means of PolSAR. *IEEE Transactions on Geoscience and Remote Sensing* 47, 2 (2009), 442–454. https://doi.org/10.1109/TGRS.2008.2009642

[19] Irena Hajnsek, Eric Pottier, and Shane R Cloude. 2003. Inversion of surface parameters from polarimetric SAR. *IEEE Transactions on Geoscience and Remote Sensing* 41, 4 (2003), 727–744.

[20] Donny Huang, Rajalakshmi Nandakumar, and Shyamnath Gollakota. 2014. Feasibility and limits of wi-fi imaging. In *Proceedings of the 12th ACM conference on embedded network sensor systems*. 266–279.

[21] Yongzhi Huang, Kaixin Chen, Yandao Huang, Lu Wang, and Kaishun Wu. 2021. Vi-liquid: unknown liquid identification with your smartphone vibration. In *Proceedings of the 27th Annual International Conference on Mobile Computing and Networking*. 174–187.

[22] John David Jackson. 1999. Classical electrodynamics.

[23] Wenjun Jiang, Hongfei Xue, Chenglin Miao, Shiyang Wang, Sen Lin, Chong Tian, Srinivasan Murali, Haochen Hu, Zhi Sun, and Lu Su. 2020. Towards 3D human pose construction using WiFi. In *Proceedings of the 26th Annual International Conference on Mobile Computing and Networking*. 1–14.

[24] Usman Mahmood Khan and Muhammad Shahzad. 2022. Estimating soil moisture using RF signals. In *Proceedings of the 28th Annual International Conference on Mobile Computing And Networking*. 242–254.

[25] Manikanta Kotaru, Kiran Joshi, Dinesh Bharadia, and Sachin Katti. 2015. SpotFi: Decimeter Level Localization Using WiFi. *SIGCOMM Comput. Commun. Rev.* 45, 4 (aug 2015), 269–282. https://doi.org/10.1145/2829988.2787487

[26] Dieter Landolt. 2007. *Corrosion and surface chemistry of metals*. CRC press.

[27] Jong-Sen Lee, Mitchell R Grunes, Thomas L Ainsworth, Li-Jen Du, Dale L Schuler, and Shane R Cloude. 1999. Unsupervised classification using polarimetric decomposition and the complex Wishart classifier. *IEEE Transactions on Geoscience and Remote Sensing* 37, 5 (1999), 2249–2258.

[28] Jong-Sen Lee, Mitchell R Grunes, and R Kwok. 1994. Classification of multi-look polarimetric SAR imagery based on complex Wishart distribution. *International Journal of Remote Sensing* 15, 11 (1994), 2299–2311.

[29] Jong-Sen Lee and Eric Pottier. 2017. *Polarimetric radar imaging: from basics to applications*. CRC press.

[30] Chao Li, Fan Li, Wei Du, Lihua Yin, Bin Wang, Chonghua Wang, and Tianjie Luo. 2021. A Material Identification Approach Based on Wi-Fi Signal. *Computers, Materials & Continua* 69, 3 (2021).

[31] Chenning Li, Zheng Liu, Yuguang Yao, Zhichao Cao, Mi Zhang, and Yunhao Liu. 2020. Wi-fi see it all: generative adversarial network-augmented versatile wi-fi imaging. In *Proceedings of the 18th Conference on Embedded Networked Sensor Systems*. 436–448.

[32] Xiang Li, Daqing Zhang, Qin Lv, Jie Xiong, Shengjie Li, Yue Zhang, and Hong Mei. 2017. IndoTrack: Device-free indoor human tracking with commodity Wi-Fi. *Proceedings of the ACM on Interactive, Mobile, Wearable and Ubiquitous Technologies* 1, 3 (2017), 1–22.

[33] Jian Liu, Yan Wang, Yingying Chen, Jie Yang, Xu Chen, and Jerry Cheng. 2015. Tracking vital signs during sleep leveraging off-the-shelf wifi. In *Proceedings of the 16th ACM international symposium on mobile ad hoc networking and computing*. 267–276.

[34] Xuefeng Liu, Jiannong Cao, Shaojie Tang, Jiaqi Wen, and Peng Guo. 2015. Contactless respiration monitoring via off-the-shelf WiFi devices. *IEEE Transactions on Mobile Computing* 15, 10 (2015), 2466–2479.

[35] AI Logvin. 2007. *Mathematical and physical modelling of microwave scattering and polarimetric remote sensing: monitoring the Earth's environment using polarimetric radar: formulation and potential applications*. Vol. 3. Springer Science & Business Media.

[36] Junqi Ma, Zhaoxin Chang, Fusang Zhang, Jie Xiong, Beihong Jin, and Daqing Zhang. 2022. Mobi2Sense: enabling wireless sensing under device motions. In *Proceedings of the 28th Annual International Conference on Mobile Computing And Networking*. 766–768.

[37] Marko Malajner, Dušan Gleich, and Peter Planinšič. 2019. Material Identification Using UWB. In *2019 14th International Conference on Advanced Technologies, Systems and Services in Telecommunications (TELSIKS)*. 232–234. https://doi.org/10.1109/TELSIKS46999.2019.9002328

[38] Kazuo Ouchi. 2013. Recent trend and advance of synthetic aperture radar with selected topics. *Remote Sensing* 5, 2 (2013), 716–807.

[39] Anurag Pallaprolu, Belal Korany, and Yasamin Mostofi. 2022. Wiffract: a new foundation for RF imaging via edge tracing. In *MobiCom'22*. 255–267.

[40] David M Pozar. 2011. *Microwave engineering*. John wiley & sons.

[41] Paul C Proffitt and Honggang Wang. 2018. Static object Wi-Fi imaging and classifier. In *2018 IEEE International Symposium on Technologies for Homeland Security (HST)*. IEEE, 1–7.

[42] Kun Qian, Chenshu Wu, Yi Zhang, Guidong Zhang, Zheng Yang, and Yunhao Liu. 2018. Widar2. 0: Passive human tracking with a single Wi-Fi link. In *Proceedings of the 16th Annual International Conference on Mobile Systems, Applications, and Services*. 350–361.

[43] Yili Ren, Sheng Tan, Linghan Zhang, Zi Wang, Zhi Wang, and Jie Yang. 2020. Liquid level sensing using commodity wifi in a smart home environment. *Proceedings of the ACM on Interactive, Mobile, Wearable and Ubiquitous Technologies* 4, 1 (2020), 1–30.

[44] Fei Shang, Panlong Yang, Yubo Yan, and Xiang-Yang Li. 2022. LiqRay: non-invasive and fine-grained liquid recognition system. In *Proceedings of the 28th Annual International Conference on Mobile Computing And Networking*. 296–309.

[45] Fei Shang, Panlong Yang, Yubo Yan, and Xiang-Yang Li. 2023. PackquID: In-packet Liquid Identification Using RF Signals. *Proceedings of the ACM on Interactive, Mobile, Wearable and Ubiquitous Technologies* 6, 4 (2023), 1–27.

[46] Cong Shi, Tianming Zhao, Yucheng Xie, Tianfang Zhang, Yan Wang, Xiaonan Guo, and Yingying Chen. 2021. Environment-independent In-baggage Object Identification Using WiFi Signals. In *2021 IEEE 18th International Conference on Mobile Ad Hoc and Smart Systems (MASS)*. 71–79. https://doi.org/10.1109/MASS52906.2021.00018

[47] Wagner B Silva, Corina C Freitas, Sidnei JS Sant'Anna, and Alejandro C Frery. 2013. Classification of segments in PolSAR imagery by minimum stochastic distances between Wishart distributions. *IEEE Journal of Selected Topics in Applied Earth Observations and Remote Sensing* 6, 3 (2013), 1263–1273.

[48] Frank Stern and Charles Weaver. 1970. Dispersion of dielectric permittivity due to space-charge polarization. *Journal of Physics C: Solid State Physics* 3 (1970), 1736–1746.

[49] Chen Wang, Jian Liu, Yingying Chen, Hongbo Liu, and Yan Wang. 2018. Towards in-baggage suspicious object detection using commodity wifi. In *2018 IEEE Conference on Communications and Network Security (CNS)*. IEEE, 1–9.

[50] Hao Wang, Daqing Zhang, Junyi Ma, Yasha Wang, Yuxiang Wang, Dan Wu, Tao Gu, and Bing Xie. 2016. Human respiration detection with commodity WiFi devices: Do user location and body orientation matter?. In *Proceedings of the 2016 ACM international joint conference on pervasive and ubiquitous computing*. 25–36.

[51] Ju Wang, Jie Xiong, Xiaojiang Chen, Hongbo Jiang, Rajesh Krishna Balan, and Dingyi Fang. 2017. TagScan: Simultaneous target imaging and material identification with commodity RFID devices. In *Proceedings of the 23rd Annual International Conference on Mobile Computing and Networking*. 288–300.

[52] Wei-Chih Wang. 1986. Electromagnetic wave theory. *Google Scholar* (1986).

[53] Yichao Wang, Yili Ren, Yingying Chen, and Jie Yang. 2022. Wi-Mesh: A WiFi Vision-based Approach for 3D Human Mesh Construction. In *Proceedings of the 20th ACM Conference on Embedded Networked Sensor Systems*. 362–376.

[54] L.B. Wolff. 1990. Polarization-based material classification from specular reflection. *IEEE Transactions on Pattern Analysis and Machine Intelligence* 12, 11 (1990), 1059–1071. https://doi.org/10.1109/34.61705

[55] Chenshu Wu, Feng Zhang, Beibei Wang, and KJ Ray Liu. 2020. msense: Towards mobile material sensing with a single millimeter-wave radio. *Proceedings of the ACM on Interactive, Mobile, Wearable and Ubiquitous Technologies* 4, 3 (2020), 1–20.

[56] Kaishun Wu. 2016. Wi-metal: Detecting metal by using wireless networks. In *2016 IEEE International Conference on Communications (ICC)*. IEEE, 1–6.

[57] Binbin Xie, Jie Xiong, Xiaojiang Chen, Eugene Chai, Liyao Li, Zhanyong Tang, and Dingyi Fang. 2019. Tagtag: material sensing with commodity RFID. In *Proceedings of the 17th conference on embedded networked sensor systems*. 338–350.

[58] Yaxiong Xie, Zhenjiang Li, and Mo Li. 2015. Precise power delay profiling with commodity WiFi. In *Proceedings of the 21st Annual International Conference on Mobile Computing and Networking*. 53–64.

[59] Yaxiong Xie, Jie Xiong, Mo Li, and Kyle Jamieson. 2019. mD-Track: Leveraging multi-dimensionality for passive indoor Wi-Fi tracking. In *MobiCom'19*. 1–16.

[60] Jie Xiong and Kyle Jamieson. 2013. ArrayTrack: A Fine-Grained Indoor Location System. In *10th USENIX Symposium on Networked Systems Design and Implementation (NSDI 13)*. USENIX Association, Lombard, IL, 71–84. https://www.usenix.org/conference/nsdi13/technical-sessions/presentation/xiong

[61] Yoshio Yamaguchi, Yuki Yajima, and Hiroyoshi Yamada. 2006. A four-component decomposition of POLSAR images based on the coherency matrix. *IEEE Geoscience and Remote Sensing Letters* 3, 3 (2006), 292–296.

[62] Dawei Yan, Yubo Yan, Panlong Yang, Wen-Zhan Song, Xiang-Yang Li, and Pengfei Liu. 2022. Real-time Identification of Rogue WiFi Connections in the Wild. *IEEE Internet of Things Journal* (2022).

[63] Jianfei Yang, Xinyan Chen, Han Zou, Chris Xiaoxuan Lu, Dazhuo Wang, Sumei Sun, and Lihua Xie. 2023. SenseFi: A library and benchmark on deep-learning-empowered WiFi human sensing. *Patterns* 4, 3 (2023).

[64] Hui-Shyong Yeo, Gergely Flamich, Patrick Schrempf, David Harris-Birtill, and Aaron Quigley. 2016. Radarcat: Radar categorization for input & interaction. In *Proceedings of the 29th Annual Symposium on User Interface Software and Technology*. 833–841.

[65] Youwei Zeng, Dan Wu, Jie Xiong, Enze Yi, Ruiyang Gao, and Daqing Zhang. 2019. FarSense: Pushing the range limit of WiFi-based respiration sensing with CSI ratio of two antennas. *Proceedings of the ACM on Interactive, Mobile, Wearable and Ubiquitous Technologies* 3, 3 (2019), 1–26.

[66] Diana Zhang, Jingxian Wang, Junsu Jang, Junbo Zhang, and Swarun Kumar. 2019. On the feasibility of wi-fi based material sensing. In *The 25th Annual International Conference on Mobile Computing and Networking*. 1–16.

[67] Shengkai Zhang, Gaoyang Liu, S Wan, et al. 2021. WiImage: Fine-grained Human Imaging from Commodity WiFi. (2021).

[68] Mingmin Zhao, Shichao Yue, Dina Katabi, Tommi S Jaakkola, and Matt T Bianchi. 2017. Learning sleep stages from radio signals: A conditional adversarial architecture. In *International Conference on Machine Learning*. PMLR, 4100–4109.

[69] Yanzi Zhu, Yibo Zhu, Ben Y Zhao, and Haitao Zheng. 2015. Reusing 60ghz radios for mobile radar imaging. In *Proceedings of the 21st Annual International Conference on Mobile Computing and Networking*. 103–116.

[70] Yang Zi, Wei Xi, Li Zhu, Fan Yu, Kun Zhao, and Zhi Wang. 2019. Wi-Fi imaging based segmentation and recognition of continuous activity. In *Collaborative Computing: Networking, Applications and Worksharing: 15th EAI International Conference, CollaborateCom 2019, London, UK, August 19-22, 2019, Proceedings 15*. Springer, 623–641.